PAPER

Check for updates

Surface-anchored carbon nanomaterials for antimicrobial surfaces†

L. Giraud,[a] O. Marsan,[a] E. Dague, [ID] [b] M. Ben-Neji,[c] C. Cougoule,[c] E. Meunier,[c] S. Soueid,[a] A. M. Galibert,[a] A. Tourrette*[a] and E. Flahaut [ID] *[a]

Carbon nanomaterials (CNMs) are known for their antimicrobial (antibacterial and antiviral) activity when dispersed in a liquid, but whether this can be transferred to the surface of common materials has rarely been investigated. We have compared two typical CNMs (double-walled carbon nanotubes and few-layer graphene) in their non-oxidised and oxidised forms in terms of their antibacterial (*Pseudomonas aeruginosa* and *Staphylococcus aureus*) and antiviral (SARS-CoV2) activities after anchoring them onto the surface of silicone. We propose a very simple and effective protocol using the air-brush spray deposition method to entrap CNMs on the surfaces of two different silicone materials and demonstrate that the nanomaterials are anchored within the polymer while still being in contact with bacteria. We also investigated their antiviral activity against SARS-COV2 after deposition on standard surgical respiratory masks. Our results show that while suspensions of double-walled carbon nanotubes had a moderate effect on *P. aeruginosa*, this was not transferred after anchoring them to the surface of silicone. In contrast, graphene oxide showed a very strong antibacterial effect on *P. aeruginosa* and oxidised double-walled carbon nanotubes on *S. aureus* only when anchored to the surface. No significant antiviral activity was observed. This work paves the way for new antibacterial surfaces based on CNMs.

1. Introduction

Microbial infections, system contamination and bio-degradation due to biofilm formation have become major issues and present serious health and economic consequences.[1] These issues concern many areas, from the food industry to the medical[2] and environmental[3] fields. Bacteria produce biofilms on materials facing environmentally challenging conditions such as implantable medical devices or materials immersed in aquatic media. Biofilms, which can be considered as structured agglomerates of microorganisms contained in a self-produced matrix, are often very difficult to remove once established. Bacterial resistance to antibiotics is also widely increasing. Therefore, it is essential to develop antimicrobial materials, with other mechanisms of action, which are able to inhibit microbial proliferation. The literature provides many different solutions to process a surface to fight against microbes. This can be obtained by killing or degrading

pathogens at the surface or only by preventing biofilm formation, or more generally speaking, adhesion of pathogens, while not necessarily destroying them.[4] In most cases, antimicrobial substances (drugs, toxic metal ions – sometimes released from nanoparticles, *etc.*[5–8]) are released, which also means that this action is necessarily limited in time. Durability can thus only be achieved in the absence of release.

We propose here that carbon nanomaterials, which have attracted attention for their antimicrobial properties when used in suspension,[9,10] may still be a good option to achieve durable antimicrobial surfaces after deposition. Carbon nanomaterials (CNMs) represent a specific category of nanoparticles that are widely known due to their exceptional properties.[11] In particular, the fact that they are not soluble and exhibit a very strong chemical resistance ensures a durable action over time. Their antimicrobial properties are described in the literature, and the most widely mentioned carbon nanomaterials (CNMs) are graphene, carbon nanotubes and their oxidized forms.[12] Most studies focus on the antibacterial activity of CNMs in suspension and the mainly reported mechanisms are oxidative stress and physical damage that are induced by the nanoparticles on cells. This topic is closely related to the potential toxicity of most CNMs. For the sake of durability and to avoid potential toxicity in the case of release in the environment, it is of paramount importance to ensure that CNMs cannot leave from antimicrobial materials. There is thus growing interest in

[a]CIRIMAT, Université Toulouse 3 Paul Sabatier, CNRS, INP Toulouse, Toulouse, France. E-mail: emmanuel.flahaut@univ-tlse3.fr, audrey.tourrette@univ-tlse3.fr
[b]LAAS-CNRS, Université de Toulouse, CNRS, Toulouse, France
[c]Institut de Pharmacologie et de Biologie Structurale (IPBS), Université de Toulouse, CNRS, Université Toulouse III – Paul Sabatier (UT3), Toulouse, France

antimicrobial composites based on the inclusion of CNMs in different matrices.[12] This increasing use of carbon nanoparticles may be related to the availability of these materials; CNMs are becoming more and more affordable with the improvement of their synthesis methods. For economic reasons, it is certainly better to localise antimicrobial nanomaterials only at the surface of materials to be protected, because their antimicrobial activity can be expressed only in the case of contact. However, it may still be interesting to include nanomaterials not only at the surface, but also within a short depth to regenerate an antimicrobial surface in the case, for instance, of abrasion. Most studies in the literature deal with composites containing carbon nanomaterials embedded in a matrix, as this is the easiest way to incorporate CNMs at the surface. However, the majority of embedded CNMs are of no use as they are inaccessible. Here we propose a very simple method allowing the development of materials with carbon nanoparticles emerging from the surface while being anchored onto the matrix. This is to the best of our knowledge the first claim of such a strategy.

Ideally, CNMs should be deposited directly at the surface of a material while ensuring appropriate anchorage to prevent their release, while maintaining the possibility of direct contact with pathogens. The objective of this work is thus to propose a method to develop antimicrobial materials based on CNMs in a "safer by design" approach. The challenge is to succeed in blocking CNMs on the surface of a polymer in such a way as to avoid the loss of efficiency over time, thus overcoming any toxicity associated with release. Focusing on the interface between CNMs and microorganisms also aims to decrease the required amount of CNMs by limiting their incorporation only at the surface and not in the bulk of the material where microbes do not have access. Very few methods allowing nanoparticles to emerge from the matrix are reported in the literature.[12] In this work, we have selected airbrush deposition because of its availability, very simple use, and novelty in this application.

We compared the CNMs mostly reported in the literature[12] for their antimicrobial activity: raw and oxidized carbon nanotubes, few-layer graphene (FLG) and graphene oxide (GO). We selected double-walled carbon nanotubes (raw DWCNTs and DWCNT Ox) as a representative model for CNTs in general as they lie at the interface between single- and multi-walled carbon nanotubes. We selected silicone as the material to which these antimicrobial properties should be transferred, mainly because this polymer is often used for medical devices intended for medium-term implantation, where microbial proliferation is thus likely to become a serious issue if it occurs. This study aims to show that airbrush deposition of water-based suspensions can be used to anchor CNMs and then compare each CNM activity towards two models of nosocomial bacteria (*P. aeruginosa*, Gram-negative, and *S. aureus*, Gram-positive) in suspension or after anchoring at the surface of silicone. To widen our study, we also aimed to compare different kinds of silicone, one of them being of medical grade. Finally, as relatively little information related to the antiviral activity of carbon nanoparticles is available and in the context of the

COVID-19 pandemic, we also investigated the antiviral activity of the same CNMs against SARS-COV2. This was performed by applying the same airbrush deposition method on surgical FFP1 respiratory mask tissue, followed by a comparison of the antiviral activity with that of a commercial graphene mask. There is growing interest in the study of the antiviral properties of CNMs.[23,24] This study also compares the antiviral activities of masks spray-coated with four different kinds of carbon nanomaterials.

Briefly, our main objective is to integrate CNMs only at the surface while anchoring them to avoid unwanted release. This safer-by-design strategy, which can be achieved by a simple airbrush spray deposition method as reported here, aims to propose engineering solutions for the responsible use of nanomaterials. This work also paves the way towards more durable antimicrobial surfaces with no loss of activity with time and without the need to release toxic substances (molecules and ions).

2. Experimental section

2.1 Carbon nanomaterials (CNMs)

We used DWCNTs which we consider as a general model for CNTs. The synthesis was described elsewhere.[27] Oxidized DWCNTs (DWCNT Ox) were prepared by refluxing DWCNTs in HNO_3 (3 M) solution at 130 °C for 24 h. After cooling down to room temperature, the oxidized nanotubes were washed with deionized water (0.45 μm polypropylene filtration membrane) until neutrality. Graphene oxide (GO) was synthesised by a modified Hummers' method.[28] 30 mL of H_2SO_4 (98 wt%), 0.5 g of $NaNO_3$ and 3 g of $KMnO_4$ were added to 0.5 g of graphite into a flask and stirred 1 h at room temperature to obtain a homogeneous suspension. The mixture was then placed in a laboratory oven at 45 °C for two days. The mixture was degassed and 40 mL of deionized water was added under stirring. After 1 h, another 50 mL of deionized water was added to the mixture under stirring, then 3 g of H_2O_2 was slowly added, and 50 mL of deionized water was added again. After 2 h at room temperature, the sample was centrifuged at 4500 rpm for 10 min. The supernatant was removed and NaOH was added to the pellet until a pH of 8.5 was reached. Ultrasonic treatment was used to further exfoliate the GO nanosheets. FLG was supplied by BeDimensional (Italy) as a powder containing sodium deoxycholate, which was removed by thorough washing with deionised water (completion of the washing process was controlled by TGA). DWCNT Ox and GO are rather stable in water, as opposite to raw DWCNTs and FLG. Ultra-low viscosity carboxymethylcellulose (CMC, Fluka 21901) was added to the aqueous suspensions (deionised water) of FLG and DWCNTs, at the same weight ratio as that of the nanoparticles (1 mg mL^{-1}), to ensure a stable dispersion and stabilise the suspension. The suspensions were bath sonicated (Elmasonic S30H, 280 W, 50/60 Hz) for 30 minutes, followed by probe sonication (VibraCell 75042, 500 W, 20 kHz, tip diameter: 13 mm) for 1 minute (30%, cycles of 3 s on, 3 s off).

2.2 Silicone

We used in this work two different silicones. SYLGARD184 (S184) bi-component silicone elastomer with a ratio of 1 : 10 was purchased from Dow Corning. Its ideal polymerization conditions should not exceed 60 °C. MED4729 (MED) bi-component biomedical silicon elastomer with a ratio of 1 : 1 was supplied by Nusil. Mixed components were degassed for 30 min under vacuum, and then 0.6 g the mixture was poured into each well of a 12-well polystyrene culture plate. The spray coating of CNM suspensions was performed on fully polymerised silicone.

2.3 Surgical respiratory mask

For the assessment of antiviral properties, a standard polypropylene surgical-type surgical class respiratory mask (Securimed) and a commercial FFP2 graphene mask (Shandong Shengquan New Materials Co. Ltd Biomass graphene) were used.

2.4 Spray deposition

Carbon nanomaterials (CNMs) were deposited either on silicone or on a commercial surgical respiratory mask (FFP1, polypropylene) using an airbrush. CNMs were first dispersed in deionised water at a concentration of 1 mg mL^{-1}. In the case of the non-oxidized CNMs (DWCNTs and FLG), carboxymethylcellulose (Fluka 21901) was added at the same concentration of 1 mg mL^{-1}. Before airbrush deposition, the suspension of CNMs was bath-sonicated for 2 minutes to ensure the proper dispersion of the CNMs. A multi-well plate (filled with silicone or the surgical mask) was fixed on a stand. An air model airbrush (nozzle diameter of 0.3 mm, supplied at 2 bars with compressed air (AS18-2 airbrush compressor)) was used to spray the dispersion 20 cm away from the target and 2 mL of suspension were sprayed with regular and repeated movements over the whole surface of the plate to ensure a homogeneous deposit. The plates containing deposits on silicone were cleaned in an ultrasonic bath for 2 minutes to remove the nanoparticles not properly entrapped at the surface. In the case of CNMs deposited on mask samples, we did not apply the cleaning step.

2.5 Sample characterisation

Scanning electron microscopy (SEM) observations were performed using an FEG FEI QUANTA 250 SEM operated at 10 kV. Drops of the aqueous suspensions of CNMs were deposited on a SEM support and observations were performed directly after drying in an oven. Silver lacquer and 5 nm platinum metallization were applied to the silicone samples prior to observation. The mask samples were observed under partial vacuum (90 Pa). Transmission electron microscopy (TEM) observations were performed using a JEOL JEM 1400 ORIUS TEM operated at 120 kV. Atomic force microscopy (AFM) experiments were performed using Nanowizard III (JPK instruments Germany) and MLCT cantilevers (Brucker) in contact mode at room temperature. The probe used was systematically calibrated; the

spring constants were measured by the thermal noise method and they were found to be between 0.591 and 0.796 N m^{-1}. The measurements were carried out in quantitative imaging mode on an area of 10 × 10 μm^2 with a resolution of 256 × 256 pixels, a maximum applied force of 2 nN, a Z length of 0.28 μm and a speed of 30 μm s^{-1}.[29] The measurements on materials were performed in deionised water; a drop was placed under the cantilever on the sample surface. The data were analysed using JPK data processing software (version 6) to produce topographical maps, adhesion maps and rigidity maps. In QI mode, force curves were recorded on each pixel and height, adhesion and rigidity can be extracted from the force curves as explained elsewhere.[29,30] Raman analyses were performed using a Jobin Yvon LabRam HR800 RAMAN confocal microscope. The samples were exposed to continuous laser radiation provided by a He laser at 633 nm with a power of 8 mW. Attenuation filters, lowering the laser power by 10, were used to avoid any degradation of the materials. The samples were placed under a BX 41 Olympus microscope and focused under a ×100 objective with a numerical aperture of 0.90 which gave the system a lateral resolution of 0.858 μm (1.22× λ/O.N) and an axial resolution of 3.12 μm (4× λ/O.N^2). The maps were produced using a motorized XYZ table with an accuracy of 0.1 μm and a measurement step of 3 μm in the X- and Y- axes and 2 μm in the Z-axis. The equipment's frequency was calibrated using the order 1 line of silicon at 520.7 cm^{-1} with an accuracy of ±1 cm^{-1}. Each point spectrum was acquired using a 600 gr mm^{-1} grating with a 1 cm^{-1} spectral resolution and collected with a quantum well detector cooled to −60 °C by the double Peltier effect (CCD synapse). Each map spectrum was acquired with a time of 30 seconds and 1 accumulation. Data processing was performed using Labspec6 software. X-ray photoelectron spectrometry (XPS) analysis was performed using a Kratos Axis Ultra (Kratos Analytical, U.K.). An adhesive copper tape was used to fix the samples. The spectrometer was equipped with a monochromatic Al Kα source (1486.6 eV). All spectra were recorded at a 90° take-off angle, with an analysed area of about 0.7 × 0.3 mm. Survey spectra were recorded with a 1.0 eV step and a 160 eV analyser pass energy. The high-resolution regions were acquired with a 0.1 eV step (0.05 eV for O 1s and C 1s) and a 20 eV pass energy. A neutralizer was used to perform the recording to compensate for the charge effects. Curves were fitted using a Gaussian/Lorentzian (70/30) peak shape after Shirley's background subtraction and using CasaXPS software. The carbon C 1s peak was calibrated at 284.8 eV for C–C and C–H bonds. The specific surface area (SSA) was measured using an ASAP 2010 M (Micromeritics) after degassing at 80 °C for 20 h in a vacuum.

2.6 Microbial strains and media

Nunclon Delta surface 6-12-24 and 96-well plates (Thermo Scientific), Luria broth (LB) liquid and LB agar medium (Fisher Scientific) were used. Bacterial strains Gram-negative *Pseudomonas aeruginosa* (strain PAO1, ATCC) and Gram-positive *Staphylococcus aureus* (strain USA-300, ATCC) provided by

the Institute of Pharmacology and Structural Biology (IPBS-Toulouse) were used for antibacterial assays. All described experiments involving *Pseudomonas aeruginosa* and *Staphylococcus aureus* were entirely performed and processed in a Biosafety Level 2 (BSL-2) facility. The bacteria were preserved in glycerol stock solution at −70 °C. The bacteria were grown overnight in LB medium at 37 °C and 160 rpm. The bacteria were sub-cultured the next day by dilution overnight culture 1/50 and grown until reaching an optical density (OD) at 600 nm of 0.5–1. Afterwards, the cells were harvested by centrifugation at 5000 rpm for 10 min and washed 3 times in phosphate-buffered saline (PBS; pH 7.3) medium. The concentration of bacterial suspensions in PBS was finally adjusted to the target concentration. Viral strain SARS-CoV-2 (BetaCoV/France/IDF0372/2020 isolate kindly supplied by Sylvie van der Werf and the National Reference Centre for Respiratory Viruses hosted by Institute Pasteur (Paris, France) was used for antiviral assays. All described experiments involving SARS-CoV-2 infections were entirely performed and processed in a biosafety level 3 (BSL-3) facility.

2.7 Antibacterial tests: colony forming unit assay

The concentrations of *P. aeruginosa* and *S. aureus* were adjusted to 10^7 and 10^8 bact per mL, respectively, to first evaluate the antibacterial activity of CNMs free in suspension. These tests were performed with the incubation of 250 µL of bacterial suspension with 250 µL of CNMs suspended in PBS at a concentration of 150 µg mL^{-1} at 37 °C. Only 8 wells in the centre of a 24-well culture plate were used and the other ones were filled with PBS to avoid evaporation. The plates were covered with aluminium foil and incubated for 24 h at 37 °C under continuous stirring (160 rpm). The incubated suspensions were then diluted in PBS ($1/20^4$ and $1/20^3$ for *P. aeruginosa* and *S. aureus* suspensions, respectively) and 100 µL of adequate dilution were spread in the wells of 6-well culture plates, each filled with 4 mL of LB agar nutritive medium. Three marbles were placed in each well and the plates were shaken to spread bacteria. Next, the plates were flipped upside down, covered with aluminium foil and incubated overnight at 37 °C before finally passing to colony counting. The evaluation of the antibacterial activity of CNMs deposited on silicone was performed by incubation of 75 µL of bacterial suspension on the samples. The concentrations of *P. aeruginosa* and *S. aureus* suspensions used were 10^5 bact per mL and 10^6 bact per mL, respectively. Only the middle wells of 12-well culture plates were used and the other ones were filled with PBS to avoid evaporation. The plates were covered with aluminium foil and incubated for 24 h at room temperature. Then incubated suspensions were diluted in PBS with a factor of $1/20^2$ and 100 µL of the dilutions were spread on the wells of a 6-well culture plate, each filled with 4 mL of LB agar nutritive medium. Three marbles were disposed of in every well and the plates were shaken to spread the bacteria in the wells. Next, the plates were flipped upside down, covered with aluminium foil and incubated overnight at 37 °C before finally processing for colony counting. The counted colonies were compared with those on the control plates to evaluate the antibacterial effect. The control of the test on the CNM suspension was PBS without CNMs and the control of the tests on the spray-deposited CNMs was the silicone material alone. The data are expressed as the number of cells per mL and were analysed using ANOVA for the calculation of statistical significance between the samples. The data were analysed using one-way ANOVA with a multiple comparison statistical test. A probability of *p*-value < 0.05 was considered statistically significant. Each tested condition was prepared in triplicate and repeated in three independent experiments.

2.8 Tissue culture infectious dose 50 TCID$_{50}$ assay

First, to determine the optimal dose of virus to be used in the assay, three doses of SARS-CoV-2 (10^3, 10^6, and 10^7 PFU) were incubated in 500 µl of serum-free DMEM and the number of infectious viral particles was measured at 6 h, 24 h and 48 h by TCID50 assay. The mask samples (Fig. S5–S7†) were cut to be adapted to the size of the 24-well plate and fixed at the bottom using carbon tape to ensure the correct deposition of the viral solution on its surface. First, 10^6 infectious particles of SARS-CoV-2 in 500 µl of serum-free DMEM were deposited on the tested material for 24 h in monoplicate. A well containing the untreated material was used to test the intrinsic activity of the material. The antiviral activity of the CNMs sprayed on silicone or the mask substrate (either sprayed under the same conditions on a classical FFP1 surgical mask or using a commercial graphene mask) was evaluated with the tissue culture infectious dose 50 (TCID50) assay in quadruplets as previously described,[31] which determines the quantity of virus necessary to induce cytopathic effects on half of the Vero E6 cells. These results are expressed in TCID$_{50}$ per mL value and the student's *T*-test (*T*. test) was applied with a bilateral distribution to statistically evaluate the viricidal activity of the samples. A probability of *p*-value <0.05 was considered statistically significant. At least, three independent experiments were performed.

2.9 Cytotoxicity assay

Vero E6 cells were incubated with the different suspensions of CNMs between 1.25 and 150 µg mL^{-1} (serial dilutions of a mother suspension at 300 µg mL^{-1}) in a 96-well plate in quadruplets. After 72 h, cell death was evaluated by measuring the release of lactate dehydrogenase (LDH) into the culture medium according to the manufacturer's instructions (Takara).

3. Results and discussion

3.1 Carbon nanomaterials

SEM observations of raw DWCNTs Fig. 1(a) reveal large clusters (up to 5 microns) from which structures emerge that likely correspond to bundles of nanotubes based on this scale. The TEM observation in Fig. 1(b) also evidences the presence of bundles of carbon nanotubes (diameter of a few tens of nm (ref. 27)), although individual nanotubes are also visible.
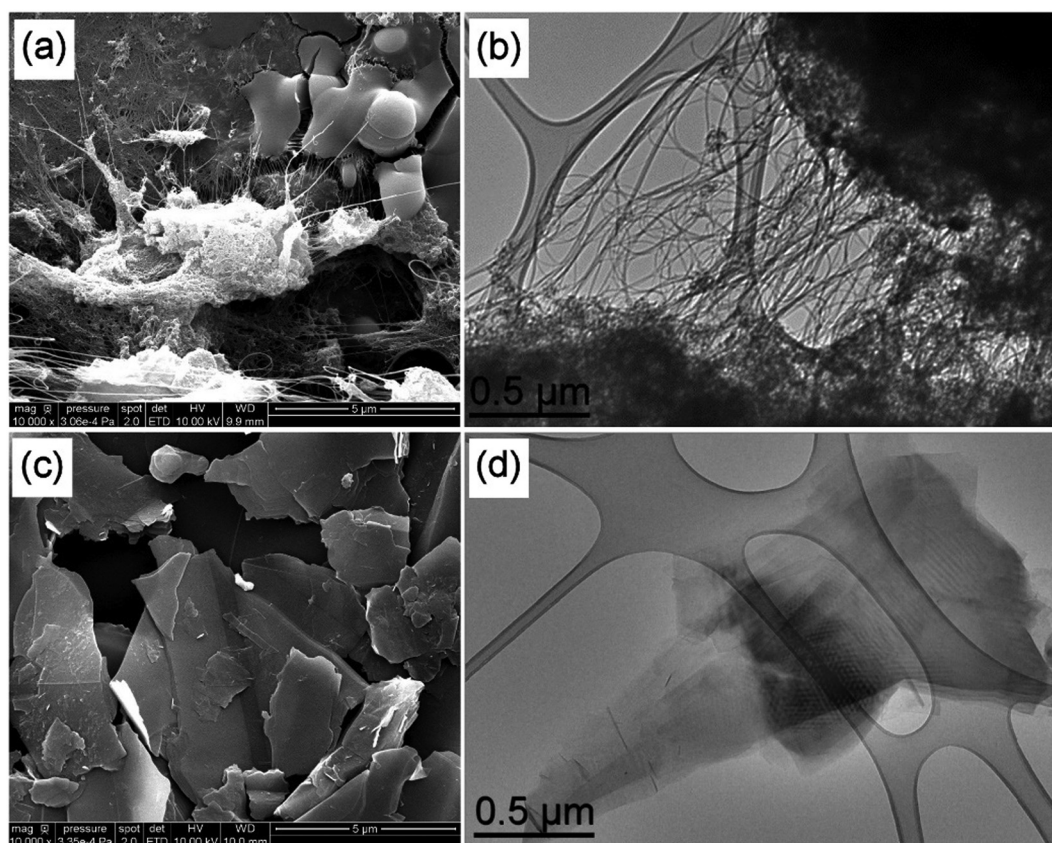
Fig. 1 SEM (scale bar 5 μm) and TEM (scale bar 0.5 μm) images of raw DWCNTs (a and b) and FLG (c and d).

Clusters of very different shapes (containing a mixture of disorganized carbon and carbon nanotubes) are observed, as well as catalyst nanoparticles that appear as very high-contrast spots.[32] Previous work has shown that the disorganized carbon clusters come from the catalytic decomposition of methane on the magnesia, which constitutes the support on which the catalytic Co : Mo nanoparticles are generated.[18] Other work has demonstrated that metal Co : Mo nanoparticles are tightly encapsulated in concentric carbon shells (carbon onions), and therefore fully inaccessible.[33]

SEM and TEM observations of FLG highlight its 2D nature, as shown in Fig. 1(c and d). The presence of superimposed sheets is clearly visible and the transparency to electrons confirm the "few-layer" nature. The lateral dimensions of the nanoparticles generally ranged between 1 and 5 microns (with a few larger particles up to 10 microns).

Oxidized DWCNTs appear more compact than raw DWCNTs in the SEM image, as shown in Fig. 2(a); this is likely to come from their more hydrophilic nature. The same observations as for raw DWCNTs may be made from the TEM image, as shown in Fig. 2(b), where large clusters and bundles of carbon nanotubes are visible. The SEM observation of GO nanoparticles highlights its 2D nature with clearly visible layers (Fig. 2(c)). As GO nanoparticles are much less conductive than FLG, metallisation was required for the SEM observation

and is visible in Fig. 2(c). Even at this low magnification, TEM observations suggest that GO is much more defective than FLG with the absence of moiré patterns and it has a "crumpled" morphology (Fig. 2(d)).

The D band at around 1330 cm^{-1} and the G band at 1590 cm^{-1} are visible in the Raman spectra of all CNMs (Fig. 3). The D band is generally associated with defects in carbon-based materials and the G band is characteristic of sp^2 carbon, the expected main hybridisation in such carbon nanomaterials. The I_D/I_G ratio (intensity ratio between the D and G bands) of raw DWCNTs is 0.26, which reflects a relatively good structural quality of these nanoparticles (Fig. 3(a)). The I_D/I_G ratio increases to 0.37 in the case of DWCNT Ox, which highlights the expected alteration of the hexagonal carbon network in these nanotubes following the oxidation step (Fig. 3(c)). RBM peaks (radial breathing modes, very sensitive to the diameter of the carbon nanotubes, between 150 and 300 cm^{-1}) can be observed for both samples, as well as the G′ peak at *ca.* 2640 cm^{-1}. We may note the attenuation of the RBM peaks in the case of oxidized DWCNTs, which is probably linked to the sample degradation. The I_D/I_G ratio is 0.10 for FLG, which reflects its very good structural quality, as can be expected from a sample prepared by graphite exfoliation (Fig. 3(b)). In the case of GO, the I_D/I_G ratio is 1.27 (Fig. 3(d)). This very high value denotes the very high structural disorder of this sample,
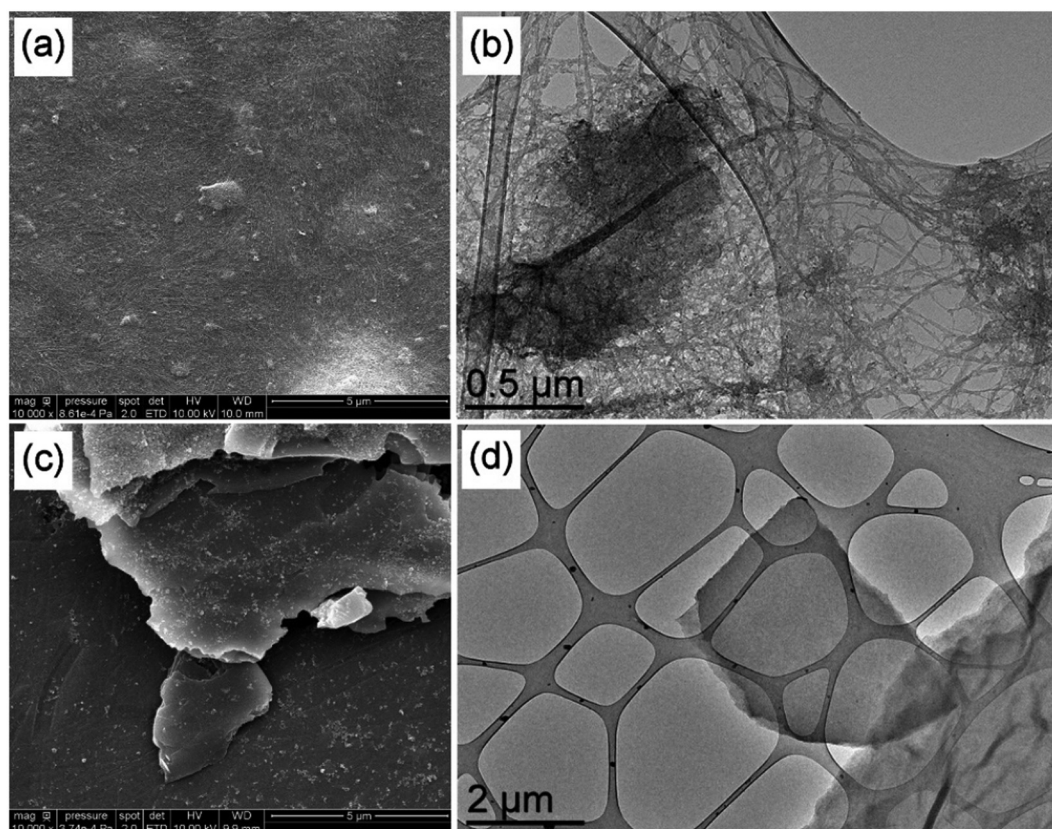
Fig. 2 SEM (scale bar 1 μm) and TEM (scale bar 0.5 μm) images of oxidized DWCNTs (a and b) and GO (c and d).
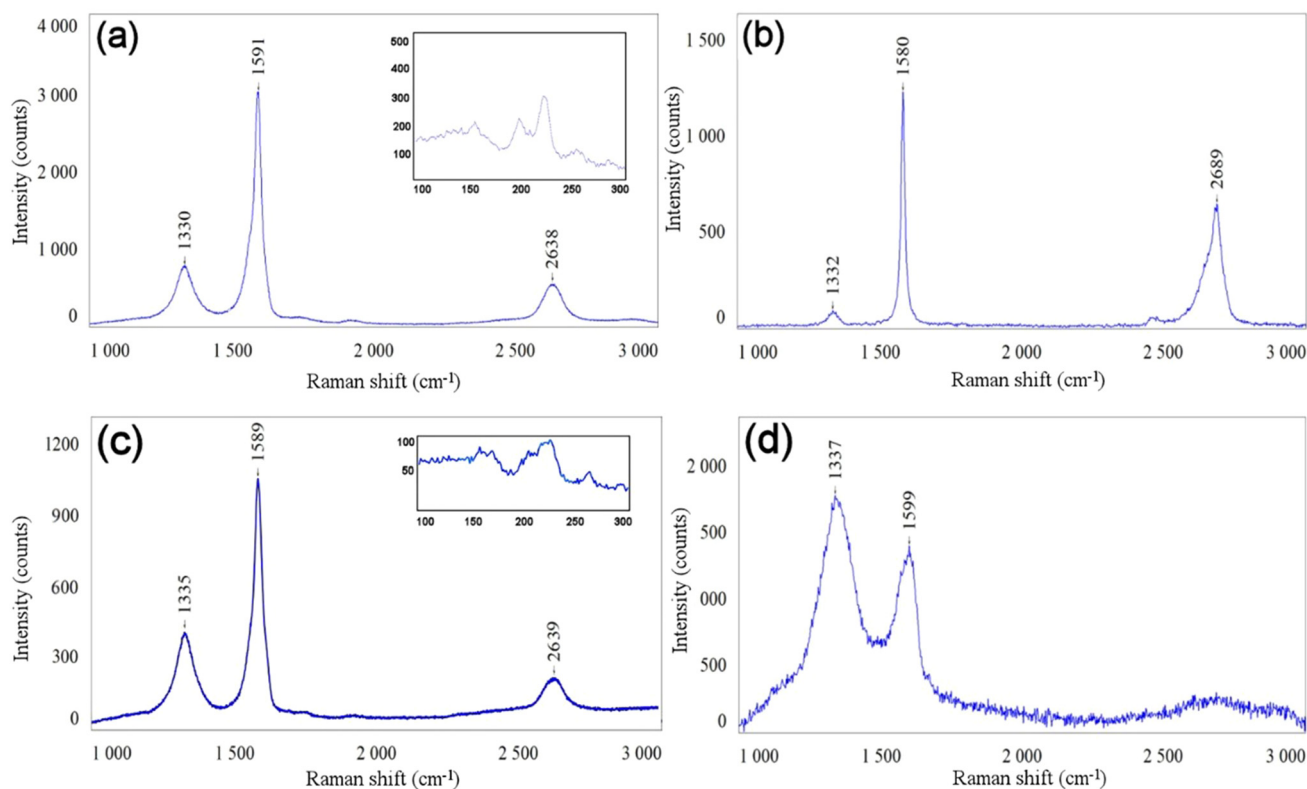

Fig. 3 Raman spectra of raw DWCNTs (a), FLG (b), DWCNT Ox (c), and GO (d). The insets in (a) and (c) show the RBM peaks. λ = 633 nm.

Table 1 Main physico-chemical characteristics of the used carbon nanomaterials: carbon mass percentages and oxygen mass percentages of raw DWCNTs, oxidized DWCNTs, FLG and GO samples from XPS analysis; size; Raman I_D/I_G ratio; and specific surface area (SSA)

	DWCNTs	DWCNT Ox	FLG	GO
C wt%	93	84	95	66
O wt%	3	15	5	29
Other elements wt%	4 (Co, Mo)	<1 (Co, Mo)	—	Traces (Mn, S)
Size	Diameter: 1–3 nm Length: 1–10 μm (bundles: diameter <50 nm; length up to 100 μm)	Identical to DWCNTs (unmodified)	Lateral size: mainly between 1 and 5 μm. Thickness: estimated <10 layers by HRTEM	Lateral size: mainly between 1 and 5 μm. Thickness: estimated <10 layers by HRTEM
I_D/I_G	0.26	0.37	0.10	1.27
SSA ($m^2\ g^{-1}$)	980	504	3–4	8

as seen in the TEM image (Fig. 2(d)). Elemental analysis (contents of carbon and oxygen) was obtained by XPS (Fig. S1 and S2†). Characterisation data for the four CNMs are summarized in Table 1.

3.2 CNMs after airbrush deposition on silicone

SEM observations (Fig. S3†) of the silicone materials after airbrush deposition of a control CMC solution in deionised water at the same concentration used to stabilise non-oxidised CNMs (DWCNTs and FLG) not only clearly evidence the presence of CMC particles at the surface, but also their full removal following the 2-minute ultrasound treatment performed on samples after airbrush deposition (flat and clean surface). Low-magnification SEM observations were performed on the samples and numerous clusters of CNMs were observed on the surface and appeared to be homogeneously dispersed (Fig. S4†). The modulation of the airbrush flow rate only increased the spot size (Fig. S4b†), but had no influence on the presence of the deposit at the surface of silicone following bath sonication cleaning. The pressure of the equipment used in this work could not be modulated. The resolution of SEM is not enough to distinguish individual CNM particles and only bundles/agglomerates may be observed. The presence of the former may thus not be excluded.

Carbon nanotube agglomerates were observed on the surface of both silicones (raw DWCNTs: Fig. 4(a and b) and DWCNT Ox: Fig. 4(c and d)). Bundles of carbon nanotubes present within these agglomerates are visible. These observations correspond to the ones of the DWCNT agglomerates, as shown in Fig. 1(b), or DWCNT Ox, as shown in Fig. 2(b), where clusters and bundles of the nanotubes were already evidenced. CNMs seem to emerge from the silicone while being partly embedded. Similarly, FLG (Fig. 4(e and f)) and GO (Fig. 4(g and h)) nanoparticle clusters are also observed at the surface of both silicones. Graphitic layers may be discerned on all these samples and also seem to emerge from the silicone. SEM observations were performed after the 2-minute bath sonication cleaning step; it is therefore assumed that they are properly anchored at the surface of both silicone materials.

To confirm this hypothesis, AFM measurements were carried out and an example is shown for GO deposited on

both silicones (Fig. 5), while the AFM data for other CNMs are presented in the ESI† (Fig. S9–S12†). Force curves were recorded according to a matrix of 256 × 256 positions on an area of 10 × 10 μm². Multiple parameters may be extracted from each force curve,[34] including the surface topology, adhesion force and curve slope that provide information on the rigidity of the sample. Topology, adhesion maps and rigidity maps can thereafter be reconstituted from these measurements, where the intensity of the parameters is represented by a colour scale (Fig. 5). To complete these maps, these values (65 536 per map) were grouped into histograms to study their distribution on the different analysed materials. AFM measurements performed on SYLGARD184 (S184), a silicone reference sample with a uniform smooth surface. The absence of colour changes in the different maps produced (Fig. 5(a–c)) evidences that there is no variation in the height, adhesion and slope of the analysed surface. This information is confirmed by the height profile and the histograms produced from the recorded force curves (Fig. 5(d–f)). The height profile of a cross-section of the sample surface (Fig. 5(d)) indicates a very smooth surface with a rather small variation in the height, less than 5 nm. The histograms show that all the values are grouped, which means that there is no variation in the data. The data obtained for the MED silicone (without any deposit), CMC control on S184 (after washing), and CMC control on MED (after washing) materials are not shown but were equivalent to those obtained for S184. No variation in the height, adhesion and slope was observed on these samples surfaces which were all smooth and uniform.

The maps obtained for the GO deposit on silicone samples confirm the presence of clusters of nanoparticles on the surface of both materials (Fig. 5(g and m)). The height maps along with the height cross-section data indicate that the GO nanoparticles are situated above the silicone surface. Different situations are observed regarding the adhesion and slope measured values for the GO clusters present on both silicones. The GO nanoparticles on S184 maps present a wide range of adhesion (Fig. 5(h and k)) and slope (Fig. 5(i and l)) values, much larger than observed on the maps of the control S184 material (Fig. 5(e and f)). The situation illustrated in the case of GO/MED is rather different with a much narrower
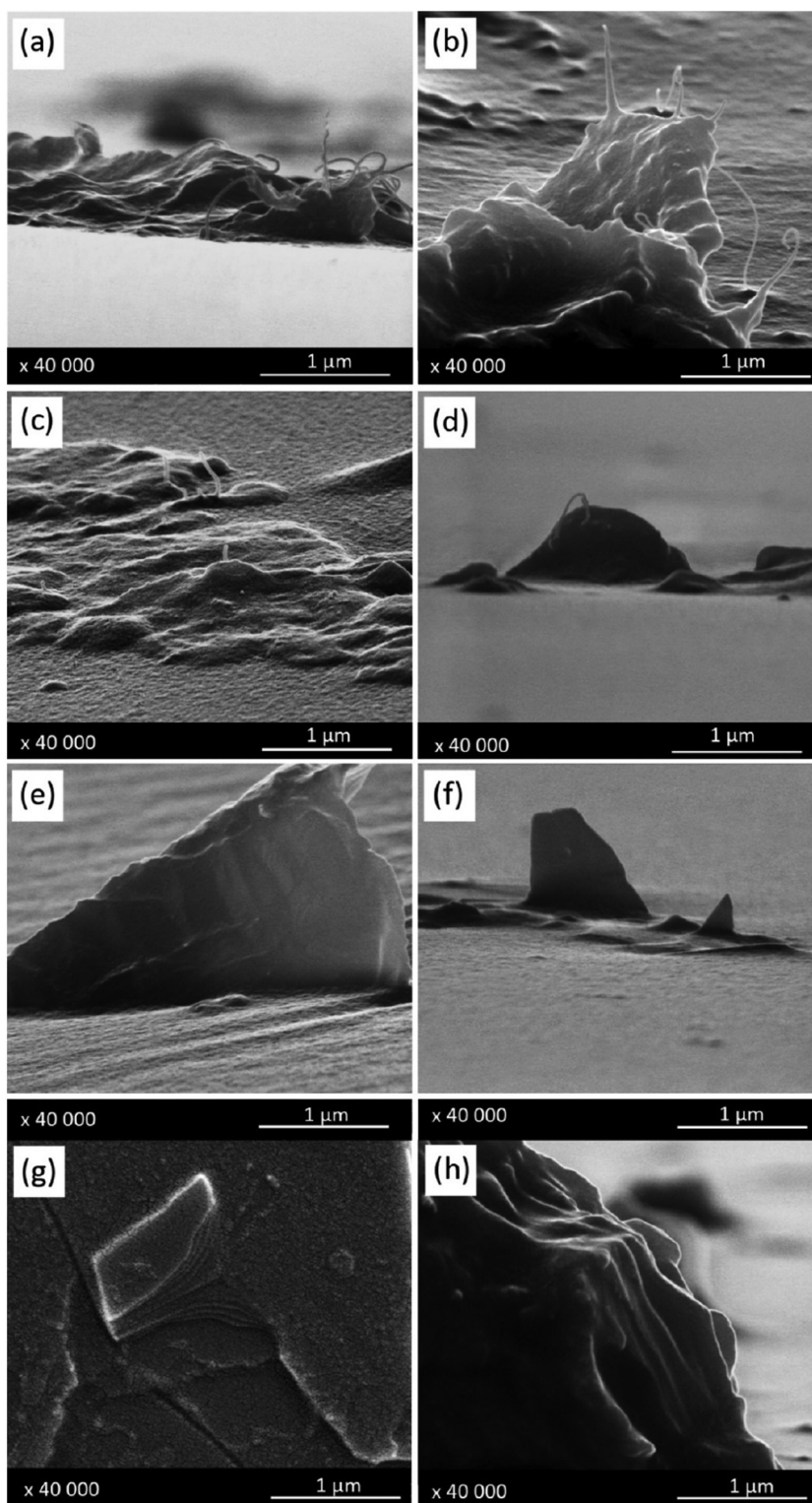
Fig. 4 SEM images of CNMs on silicone materials: (a and b) DWCNTs, (c and d) DWCNT Ox, (e and f) FLG, and (g and h) GO on silicone: left column (a, c, e and g) silicone S184; right column (b, d, f and h) silicone MED.

range of adhesion distribution and a bimodal distribution of the slope. While we have shown typical examples of each deposit of the two different silicones, rather different situations were observed, but all indicating that GO agglomerates are definitely anchored in both silicones. The widening of the distribution of both the adhesion force and slope also illustrates that many more different cases may be encountered where the particles may be covered with a variable thickness of
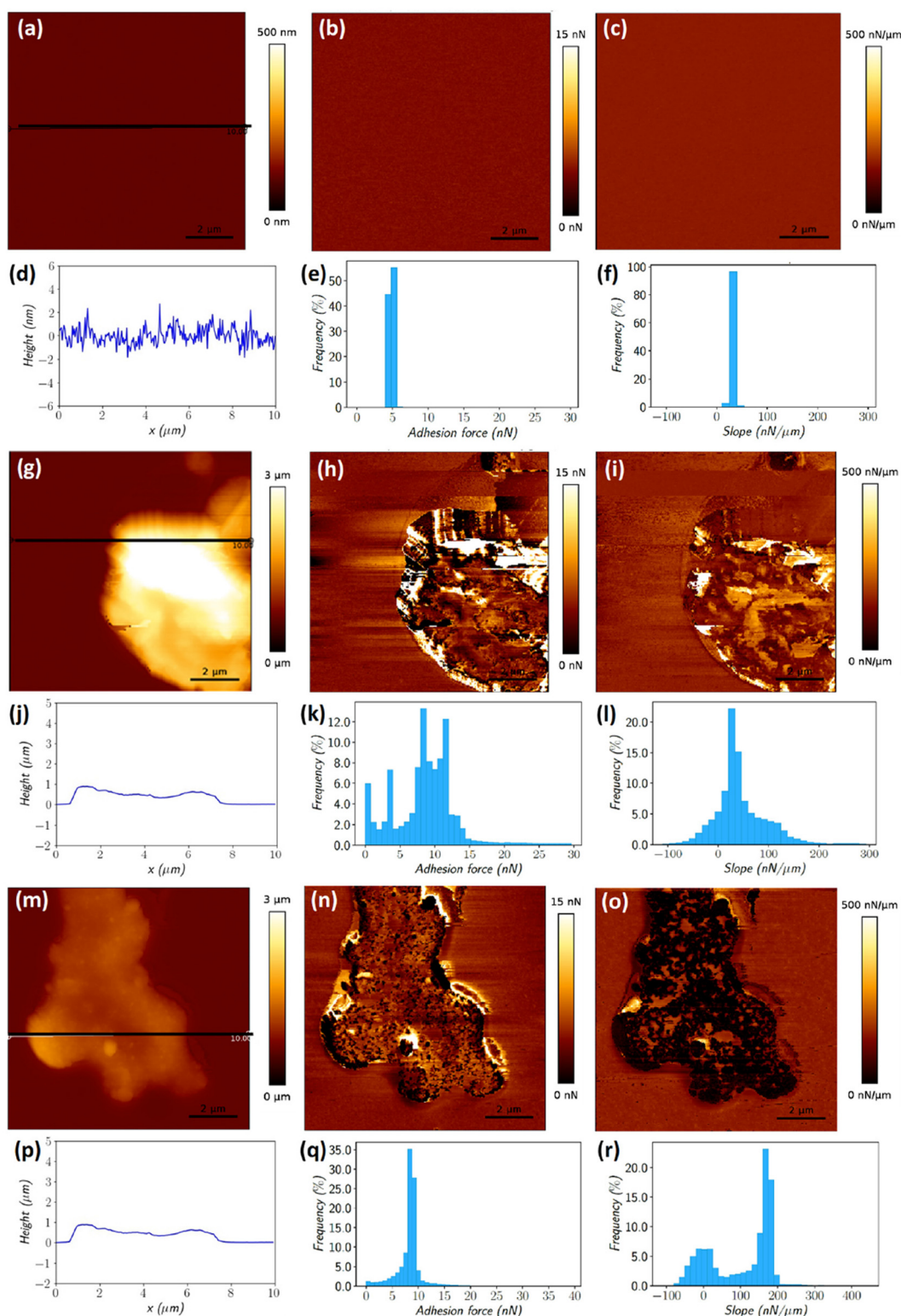
Fig. 5 AFM multiparametric imaging (topography, adhesion and rigidity) of silicone S184 reference (a–f), GO/S184 (g–l) and GO/MED (m–r): (a, g and m) height maps; (b, h and n) adhesion maps; (c, i and o) slope maps; (d, j and p) height cross-sections; (e, k and q) adhesion distribution histograms; and (f, l and r) slope distribution histograms.

silicone, or even no silicone at all, or may finally be located more or less deep in the silicone. Similar observations were made on the other samples (deposits of DWCNTs, DWCNT Ox and FLG). Fig. 5 only shows a selection of representative images (Fig. S9–S12† are provided as other examples).

Spatially-resolved 3D (confocal) Raman micro-spectroscopy mappings were carried out on the GO/S184 (Fig. 6(b)) and GO/MED samples (Fig. 6(d)). The analysed surface and the Z amplitude of the samples were selected to obtain clusters of the nanoparticles of several sizes to study different configurations (Fig. 6). For all the spectra, the Raman signals (point analyses or maps) characteristic of the G band (sp^2) of GO at 1530 cm^{-1} and the C–H bands of silicone at between 2800 cm^{-1} and 3100 cm^{-1} were respectively integrated into each point. The red and green colours were chosen to identify the integration of the bands of GO and silicone to create 3D distribution maps of the two deposits of GO on S184 and GO on MED. The spatially resolved maps in 3 dimensions show particles randomly distributed above the surface and inside the matrix. There are different configurations with nanoparticle clusters of different sizes that seem to be more or less submerged in the polymer and emerging from the surface, whatever the silicone used.

Raman analyses were carried out at a localised point situated on a GO cluster on the surface of the samples (Fig. 6(e and g)). To obtain information about the anchoring of the nanoparticles in the silicone and also if they are emerging from it, several spectra were recorded at this point along the z-axis with an amplitude ranging from +3 μm to −10 μm with respect to the zero plane (Fig. 6(f and h)). These analyses were

carried out on both GO/silicone samples. The depth profiles clearly show in both cases that the GO agglomerates not only emerge from the surface, but are also embedded in the silicone. It seems that the ratio between the relative intensities of GO and silicone peaks gradually reverses as the depth of the polymer increases.

Spatially-resolved 3D (confocal) Raman micro-spectroscopy mappings were also carried out on the DWCNT Ox/S184 (Fig. 7(a and b)), and DWCNT Ox/MED (Fig. 7(c and d)) samples. As before, the analysed surfaces and Z amplitudes of the samples were selected to present clusters of the nanoparticles of several sizes to study different configurations. In all the Raman spectra, the G′ band at 2650 cm^{-1} and the C–H stretching band at 2960 cm^{-1}, which are Raman characteristics signals of DWCNT Ox and silicone respectively, were integrated (we chose to integrate the bands of equivalent sensitivity). The maps show clusters of nanoparticles randomly distributed on the surface and inside the polymer. These clusters seem more or less immersed in the silicone and the two maps represent clusters emerging from the silicone surface.

The comparison of data obtained from three different characterization methods carried out on the samples allows us to conclude that airbrush deposition of water-based CNM inks is an effective way to anchor these nanomaterials at the surface of silicone. The different characterization methods complement each other and evidence the clusters of nanoparticles (where bundles and platelets may be distinguished) that are both anchored and emerging from the matrix. It differs from most studies in the literature where CNMs are fully embedded in the support (nanocomposites) or simply de-
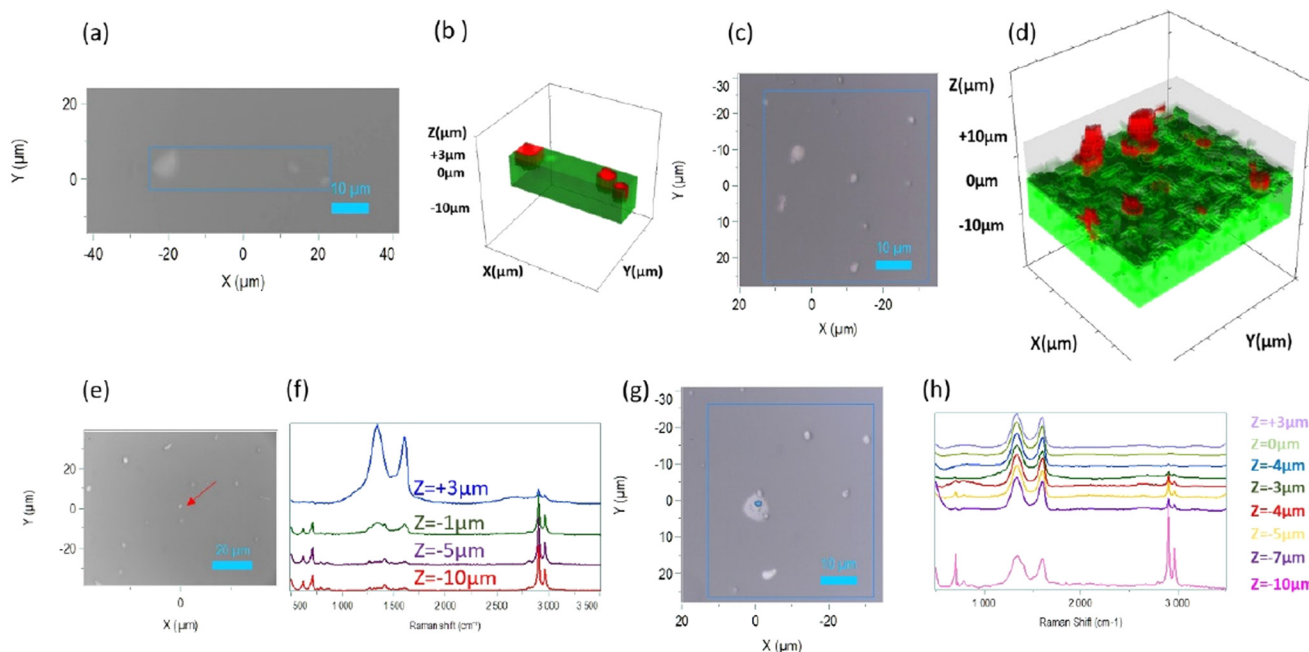

Fig. 6 Raman analysis of GO on silicone: (a and c) 2D optical images with a boxed location and (b and d) corresponding 3D Raman maps with silicone depicted in green and the emerging GO represented in red. (e and g) 2D optical images with a boxed location and (f and h) corresponding confocal analysis; (a, b, e and f) GO/S184 and (c, d, g and h) GO/MED.
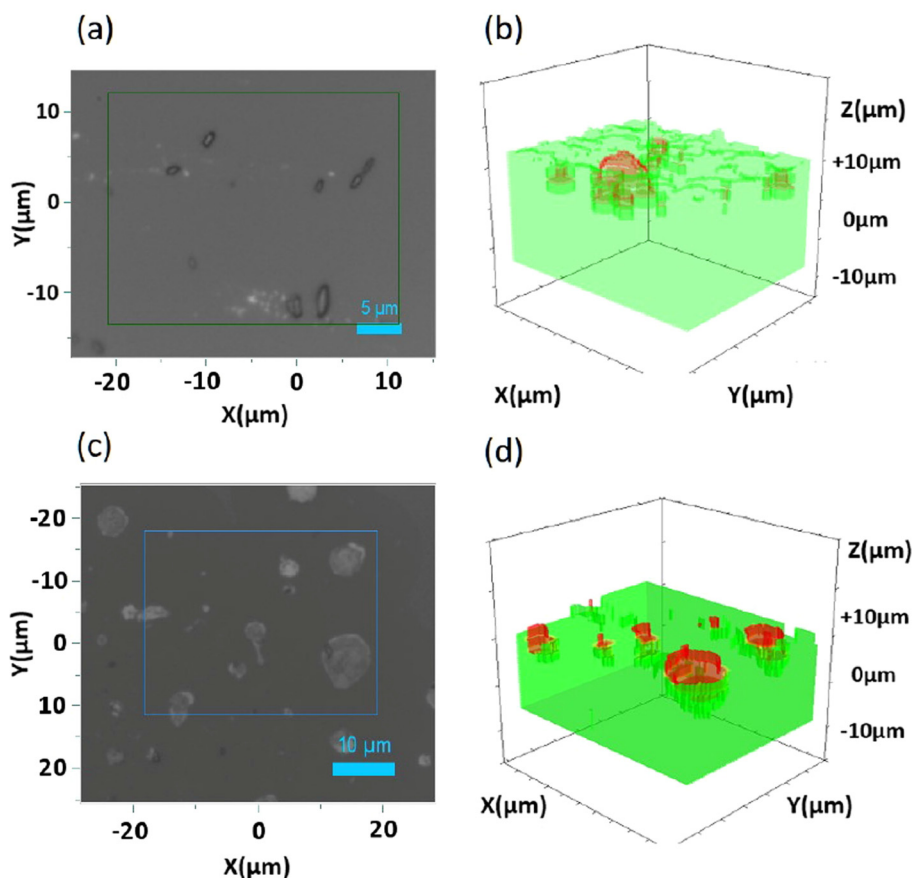
Fig. 7 Raman analysis of DWCNT Ox on silicone: (a and c) 2D optical image with a boxed location and (b and d) corresponding 3D Raman maps with silicone depicted in green and the emerging DWCNT Ox represented in red; (a and b) DWCNT Ox/S184 and (c and d) DWCNT Ox/MED.

posited with no evidence of efficient anchoring. The fact that only large agglomerates are visible at the surface of silicone does not exclude the presence of smaller particles in between, which are more difficult to evidence due to the resolution or sensitivity depending on the characterisation tool. This means that the amount of CNMs at the surface may be much larger than what is evidenced here.

3.3 Investigation of antimicrobial activity

3.3.1 Antibacterial activity of CNMs. Fig. 8 summarizes the experimental protocols which were used in this work (see sections 2.4–2.7).

CFU tests were performed on CNMs/silicone deposits (Fig. 8(a)) against *P. aeruginosa* and *S. aureus* bacteria (Fig. 9). None of the silicones exhibited any intrinsic antibacterial activity, indicating that even if their composition was certainly different (exact composition of commercial silicones in not possible to obtain), the possible presence of hardener residues did not have any impact. The tested suspensions of CNMs in PBS (Fig. 8(b)) did not exhibit any antibacterial activity neither on *P. aeruginosa* bacteria nor on *S. aureus* bacteria (Fig. 9(a–d)). Only the oxidised CNMs exhibited some antimicrobial activity as deposits on silicones (Fig. 9(e–l)). Among the different tested materials, deposits of GO on the silicone samples

exhibited very strong antibacterial activity against *P. aeruginosa* (Fig. 9(i and j)) but not against *S. aureus* (Fig. 9(k and l)). In contrast, deposits of DWCNT Ox exhibited a very strong antibacterial activity against *S. aureus* but not against *P. aeruginosa*. Since no antibacterial activity could be evidenced for in the presence of non-oxidized CNMs, we cannot exclude the presence of traces of adsorbed CMC which may inhibit their possible antibacterial activity. However, as the washing steps were proved to be rather efficient, it is supposed that only limited amounts of CMC may still be adsorbed. CMC contain carboxylic functions, which are also present at the surface of oxidised CNMs.

3.3.2 Antiviral properties of CNMs. Here to quantify the viral load, we assessed the ability of the virus to kill infected cells (TCID50 assay) as previously described.[31] As in the previous investigation of the antibacterial load, it is mandatory to first check whether any CNM particles that may detach or not from the surface of the support material may exhibit a direct toxicity towards Vero E6 cells used for viral load quantification. We thus first evaluated the cytotoxicity of CNMs on Vero E6 cells. The cells were incubated with different doses of CNMs (from 1.25 to 150 μg mL^{-1}) for 3 days and toxicity was evaluated by LDH release assay. The highest concentration of 150 μg mL^{-1} would correspond to the release of all the CNMs
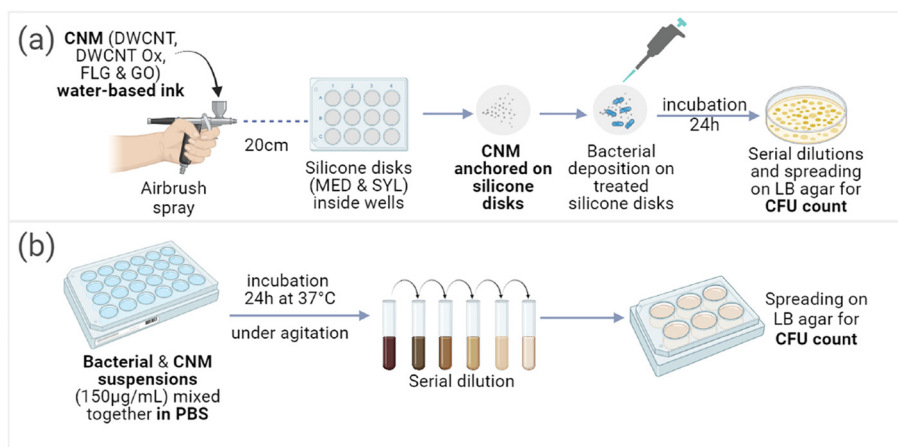
Fig. 8 Visual representation of the protocols employed to test the antibacterial activity of CNMs: (a) after anchoring on the surface of silicone disks and (b) in suspension.
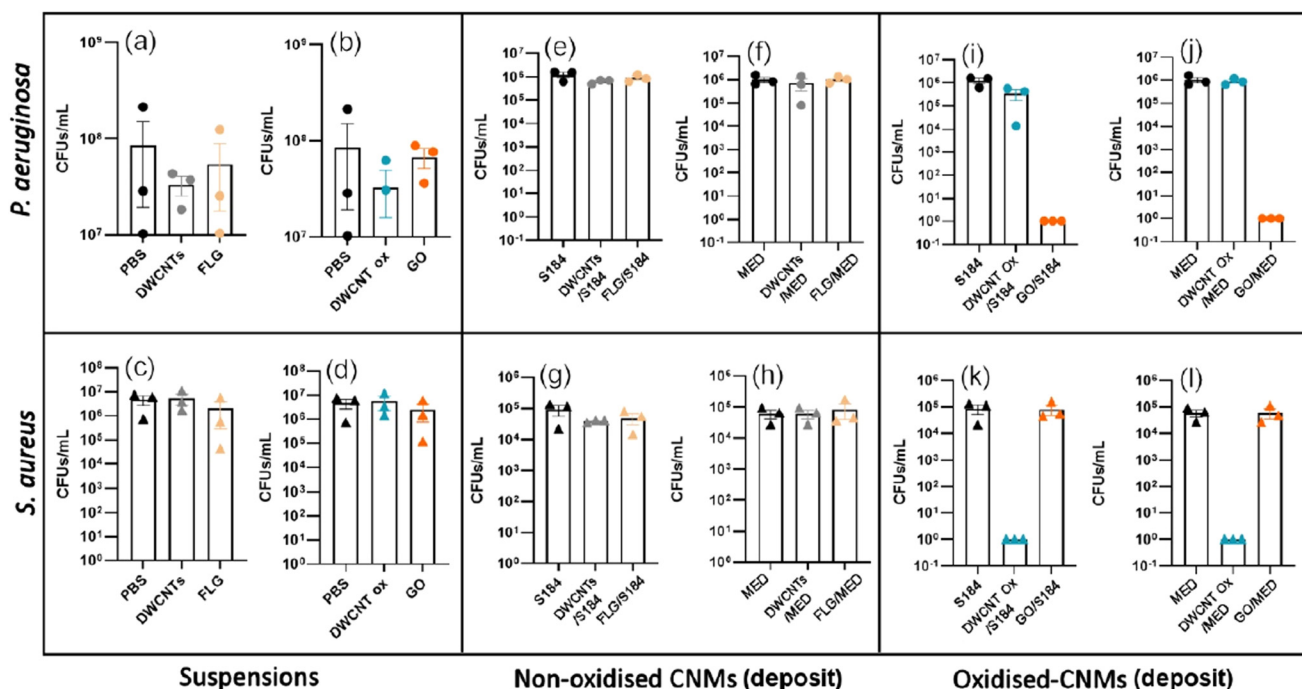

Fig. 9 (a–d) Antibacterial effect of the suspensions of CNMs (150 µg mL^{-1}) on *P. aeruginosa* of: (a) non-oxidised CNM suspension and (b) oxidized CNM suspension, and on *S. aureus* of: (c) non-oxidised CNM suspension and (d) oxidized CNM suspension. (e–h) Antibacterial effect of the deposits of non-oxidized CNMs on *P. aeruginosa*: (e) on S184 and (f) on MED, and on *S. aureus*: (g) on S184 and (h) on MED. (i–l) Antibacterial effect of the deposits of oxidized CNMs on *P. aeruginosa*: (i) on S184 and (j) on MED, and on *S. aureus*: (k) on S184 and (l) on MED. Data are illustrated as the mean of at least *n* = 3 independent experiments represented by circles for *P. aeruginosa* and triangles for *S. aureus*, with error bars indicating the SD. The colour code corresponds to different kinds of CNMs.

deposited on the material placed at the bottom of a given culture well. As shown in Fig. 10(a), none of the CNMs exhibited any toxicity towards Vero E6 cells, whatever the tested dose, which allows us to exclude any possible false positive antiviral activity. To determine the viral load to be used in our experiments, we evaluated the kinetics of SARS-CoV-2 infectivity with time. Three different doses of SARS-CoV-2 (10^3 to 10^7 PFU) were incubated for 6 to 48 h at 37 °C. The viral load was

measured by TCID50 assay. As shown in Fig. 10(b), we observed the expected decrease in the virus load over time.

From the obtained results, we decided to test the viricidal activity of CNMs with the intermediate dose of 10^6 PFU at 24 h. The CMC control corresponds to a spray of CMC at 1 mg mL^{-1} is used as a control in case of incomplete washing. As shown in Fig. 11, none of the CNMs presented any significant viricidal effect against SARS-CoV-2 on any of the tested sub-
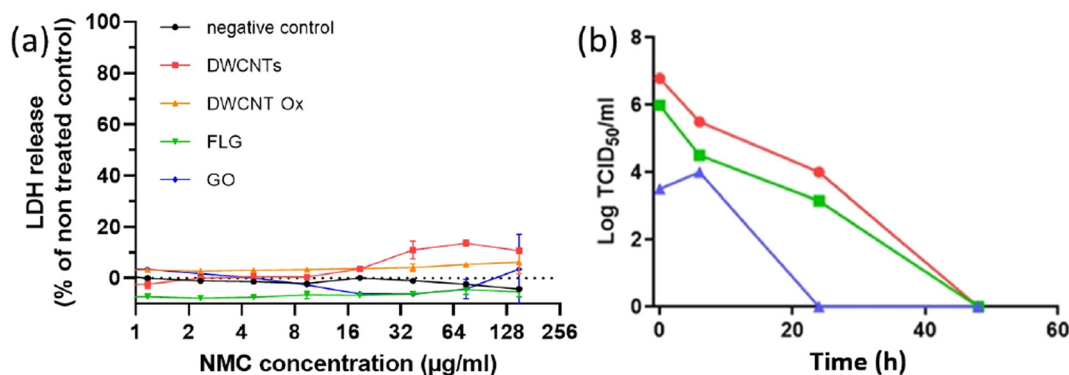
Fig. 10 (a) Cytotoxicity of CNMs on Vero E6 cells measured by LDH release assay after 3 days of incubation; data are expressed as the mean $\pm$ SD of two independent experiments. (b) Kinetics of SARS-CoV-2 load decrease *vs.* time in DMEM (red: 10^3 PFU; green: 10^6 PFU; blue: 10^7 PFU).
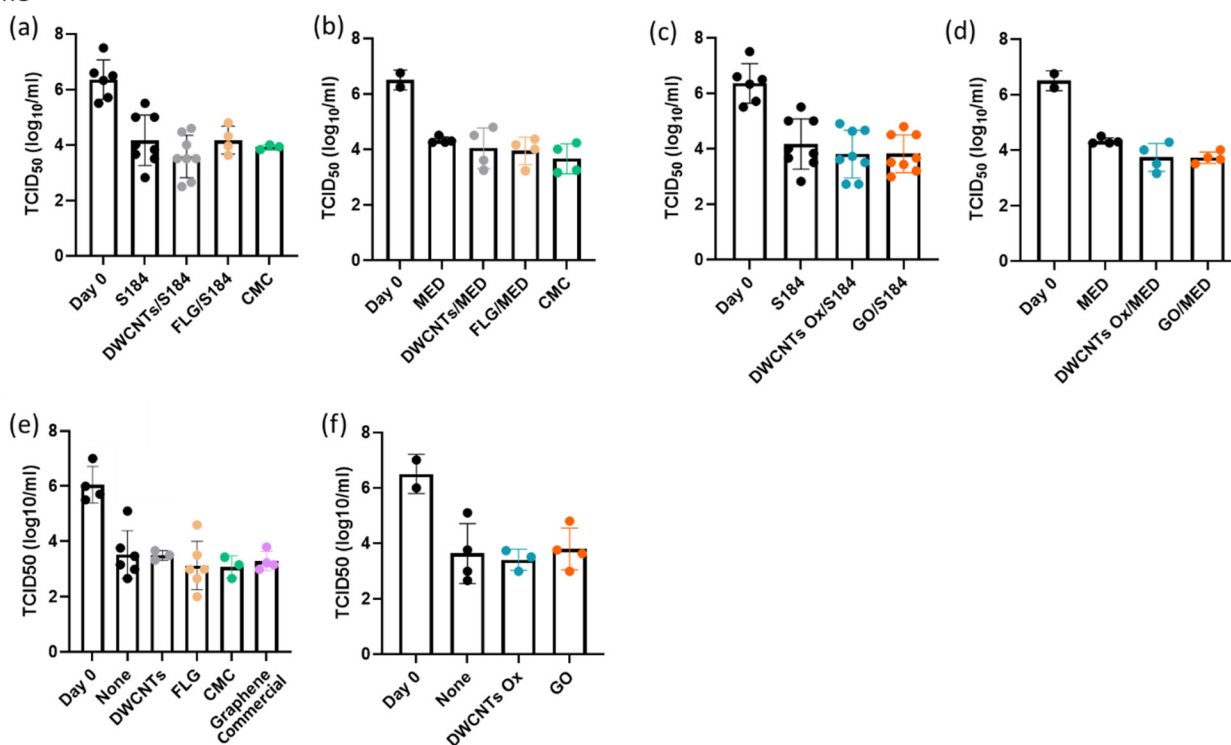

Fig. 11 Antiviral effect on SARS-CoV-2 of (a) non-oxidised CNMs deposited on S184, (b) oxidized CNMs deposited on S184, (c) non-oxidised CNMs deposited on MED, (d) oxidized CNMs deposited on MED, (e) non-oxidised CNMs deposited on a classical (FFP1) surgical mask, and (f) oxidized CNMs deposited on a classical (FFP1) surgical mask. In (e), the result of the test of the commercial graphene mask (graphene commercial) is included. Data are illustrated as the mean of at least n = 2 independent experiments represented by circles, with error bars indicating the SD. The colour code corresponds to different kinds of CNMs.

strates. The conclusion is the same for the commercial graphene mask that we have tested as a comparison (Fig. S6–S8†).

3.4 Discussion

The different characterization methods performed on the materials after 2 min of ultrasound cleaning complement each other. At both low and high magnifications, SEM observations showed clusters and bundles or platelets of CNMs homogeneously dispersed on the material surface. AFM analysis revealed all possible configurations with small clusters with an elevation of *ca.* 100 nm from the silicone surface, whereas some bigger clusters presented an elevation of around 1 μm from the silicone surface. Raman analyses proved that the CNM clusters were both blocked and emerging from the surface. Several elaboration methods are reported in the literature for the development of antimicrobial composites based

on CNMs, such as electrospinning,[13–15] 3D printing,[16–18] dip coating,[19,20] *etc.* However, these nanocomposites contain the nanoparticles within the whole matrix. Very few methods allowing CNMs to emerge from a polymer matrix are described in the literature and are usually based on the removal of the matrix at the top surface of a nanocomposite. As an example, a UV/O$_3$ oxidation treatment on GO nanosheets allowed etching away the surface polymer (2-hydroxyethyl methacrylate (HEMA)) and direct access to the nanoparticles was reported.[21] Another mentioned method is laser ablation which was able to resurface GO nanoparticles embedded in an agarose matrix by liquefaction and matter transport.[22] Hence, we have demonstrated in the case of silicone that CNMs may be transferred effectively at the surface using airbrush deposition, and we have also shown that the dispersant required in the case of non-oxidised CNMs to prepare a stable suspension could be removed by 2 min bath-sonication cleaning in water, while keeping the CNMs anchored at the surface of the coated material.

Our results show that after deposition on silicone, only GO had a strong impact, and only on *P. aeruginosa*, while only oxidised DWCNTs had a strong impact on *S. aureus*. The majority of studies suggest the antimicrobial mechanisms of CNMs after employing techniques such as SEM (to identify morphological changes) and staining, followed by fluorescence microscopy.[51–53] These mechanisms cannot be universally applied, as this greatly depends on the physical characteristics of the CNMs employed (such as structure, specific surface area, length, diameter, and the presence of functional groups on the surface).[51,54] However, it is globally assumed that CNMs exert their antimicrobial activity based on three modes of action: through mechanical stretching or piercing, physical interaction with the cell membrane, resulting in wrapping and isolation from its nutritive surrounding, and/or through the generation of reactive oxygen species (ROS), resulting in oxidative stress, thus disrupting the bacterial cell membrane (due to lipid peroxidation).[51,55,56] It is worth noting that only oxidised materials exhibited antibacterial activity after deposition on silicone, while none of them had any activity on the same bacteria in suspension. This suggests that the presence of the oxygen-containing groups present at the surface plays a major role.

In the case of the deposited CNMs, the washing step proved to be effective for the removal of surface CMC also deposited together with CNMs (Fig. S3†), although the total removal of CMC is both difficult to assess and relatively unlikely. These observations suggest that not only the shape of the CNMs is important, but also their surface chemistry. The surface of oxidised CNMs being much more chemically reactive and may induce higher levels of oxidative stress within bacteria after interaction with the membranes. Gram-negative bacteria have a thin peptidoglycan layer of 6 to 15 nm and an additional outer lipid membrane, whereas Gram-positive bacteria have a thick peptidoglycan layer of 20–80 nm and miss the outer lipid membrane. Thus, the test results may be related to the differences between the cell walls of Gram-positive and Gram-negative bacteria and the different morphologies between the

tested CNMs. For example, it has been reported that Gram-positive bacteria such as *S. aureus* may be more susceptible to the piercing effect of needle-shaped CNTs,[57] while Gram-negative *P. aeruginosa* is assumed to be more susceptible to the 'nano knife' and wrapping effect of GO. In addition, the shape of the bacteria may also impact the selectivity of CNMs, and CNTs may have more effect against spherical-shaped *S. aureus* bacteria than rod-shaped *P. aeruginosa* bacteria.[48] However, it is difficult to conclude on the active mechanisms in this study through literature analysis as the available literature can be contradicting. For example, Rogala-Wielgus and Zieliński argue in their state of art that in contrast to Gram-positive bacteria, Gram-negative bacteria such as *P. aeruginosa* and *E. coli* are more susceptible to the piercing effect of CNTs.[56] In addition, Diez-Pascual suggests that membrane harm induced by GO is more damaging towards Gram-positive bacteria than Gram-negative bacteria.[55]

Our results show that the initial assumption that CNMs active in suspension would also be active after deposition on a surface was obviously not correct. The difference between these two configurations may come from their mobility. CNMs incubated with bacteria in suspension can move freely within the volume, potentially resulting in less direct contact between the two, whereas CNMs fixed on the silicone surface resulted in enhanced contact with the microorganisms, as the bacterial suspension was directly deposited on the treated surface. We also show that GO and oxidised DWCNTs exhibited the same antibacterial activity on both silicones, suggesting that the airbrush coating method may be used on several different supports to elaborate CNM-based antimicrobial surfaces. This hypothesis will be investigated in further works. As mentioned previously, although the exact antibacterial mechanisms were not investigated in this preliminary work, AFM will be used to investigate the mechanical impact of the tested materials on microorganisms.[29,49,50] Damage to cell membranes by the generation of reactive oxygen species (ROS) will also be investigated using markers of lipid peroxidation.[20] In addition, the proportion of live and dead bacteria will be evaluated by fluorescence measurements (live–dead assay) and compared to SEM images to assess the distribution of CNMs at the surface and the morphology of the exposed bacteria. The size of the investigated bacteria in this work is typically between 0.5 and 5 μm, *S. aureus* being slightly smaller than *P. aeruginosa*. The images of the surface of silicone after spray deposition all show rather larger agglomerates, which are separated by distances that look larger than the size of the bacteria. However, as already discussed, it is likely that smaller agglomerates, or even individual particles, may also be present in between. The contact-killing hypothesis should thus still be valid.

Finally, in the context of the COVID-19 pandemic, graphene and related materials have attracted attention with the commercialization of graphene-based respiratory masks, claimed to exhibit some viricidal activity. Previous work has already been performed and reported antiviral activity against SARS-CoV-2 from masks spray-coated with carbon nanotubes and masks with a carbon nanotube filter.[25,26] However,

although the principle of coating a surface with a CNM by spray-deposition was indeed the same, it must be noted that the role of the used CNM (carbon nanotubes) was mainly to bring superhydrophobicity in the work of Soni et al.,[25] which is not the case in this work, for none of the investigated CNMs. They also used a benzene-based ink, while we developed a water-based approach. In the work of Lee et al.,[26] CNTs were directly integrated in dry form using a very specific approach which cannot be generalised to other commercial sources of carbon nanotubes. Our results with two different morphologies (1D and 2D) and two different surface chemistries (oxidised CNMs or not) have not revealed such effect against SARS-COV2, whatever the tested support on which they were deposited (silicone or respiratory mask). In this preliminary work, we have not checked the possible release of CNMs in the medium, possibly leading to false results. However, we checked that the incubation of Vero E6 cells at concentrations higher than what could be achieved in case of the total release of deposited CNMs had no impact on these cells. This allows us to rule out any possible interference. As in the case of the investigation of antibacterial activity, this work will require more in-depth investigations (in progress). However, the absence of viricidal activity in the commercial mask is still valid and raises questions.

Although the antimicrobial impact of CNMs has been largely described in the literature, most works were dealing with direct contact with particles in suspension in the exposure medium.[20,35–38] This work focused on investigating the antimicrobial activity of the elaborated materials against Gram− type P. aeruginosa and Gram+ type S. aureus bacteria by measuring the capacity of bacteria to form colonies after incubation with the materials. No antimicrobial activity from the different CNM suspensions was evidenced from our work. These results are in contradiction with some earlier publications dealing with similar CNMs. However, the large variability in terms of results may also easily be explained by the differences in terms of the CNMs themselves, the tested concentrations and experimental conditions (duration, medium composition, etc.). This is the main reason why we decided in this work to investigate simultaneously two monodimensional (1D) and two bidimensional (2D) morphologies, including the as-produced and an oxidised form, to include this very important aspect. Indeed, the oxidation of CMN typically increases significantly the stability of suspensions in aqueous medium, which leads to increased impact due to better interaction with the cells. In our work, we have added CMC, a food additive (E466), to suspensions of non-oxidised CNMs (DWCNTs and FLG) to overcome the stability issue after checking that the dispersant itself did not have any impact. This issue was recently discussed in the framework of OECD test guidelines for the environmental impact of graphene and related materials, where the addition of a dispersant is accepted.[39] This appears in contradiction with our earlier work on the same non-oxidised DWCNTs in which a moderated activity towards P. aeruginosa was demonstrated using the same assay at similar concentrations of both CNMs (100 μg mL^{-1}, while we used 150 μg mL^{-1} in this work) and bacteria for the same exposure duration of 24 h. Furthermore, in this same work, we described a very strong activity against S. aureus that we have not reproduced here. The only difference between these 2 works is the presence of CMC in this work (which does not exhibit any intrinsic antibacterial activity), which would suggest that a better dispersion does not help to fight against P. aeruginosa and S. aureus. However, the antibacterial activities of both GO and rGO in suspension were reported by Gurunathan et al. against P. aeruginosa via oxidative stress induction,[40] while the exact bacterial concentration is unknown. The ability of CNTs to inhibit the proliferation of S. aureus was also reported.[35,41] These contradictory results may be explained not only by the differences between the CMN themselves, but also between all the other experimental parameters, including the way the CFU assay was performed.[41–43]

In this work, our initial work hypothesis was that if some antimicrobial activity was observed with CNMs in suspension, it should be transferred to the surface of a material after coating with the same suspension based on the commonly accepted assumption that the main antimicrobial mechanisms associated with CNMs involve direct contact with the microorganisms. This direct contact is not possible when CNMs are included within a matrix making up a nanocomposite. A few methods have been proposed in the literature to prepare antimicrobial composites based on carbon nanomaterials but they mostly describe fully embedded nanoparticles into the polymeric matrix.[44–47] Rare approaches allowing a direct access to CNMs embedded in a polymer may be found, such as the use of a UV/O$_3$ oxidation treatment to etch away the surface polymer or the use of laser ablation that allows embedded nanoparticles to resurface from the matrix.[21,22] This work has thus focused on blocking the carbon nanoparticles on a polymeric surface while also allowing them to emerge from this surface to enable direct contact between microorganisms and CNMs while ensuring the durability of action without the loss of nanoparticles and no toxicity issue related to the released nanoparticles.

4.   Conclusion

We have shown that airbrush coating is a suitable method to obtain elaborate CNM-based antimicrobial surfaces on silicone compared to the two most investigated carbon nanomaterials, carbon nanotubes and few-layer graphene. Because surface chemistry usually plays a major role, we also included their oxidised counterparts. Characterisation of the deposits combining SEM, AFM and Raman spectroscopy 3D mapping demonstrates that airbrush coating allowed anchoring of all the tested CNTs at the surface of two different silicone materials used in very different fields of applications (microfluidics and coating of electronics for Sylgard 184, and the biomedical field for MED-4729). An investigation of the antimicrobial activity of CNM-coated surfaces was also performed: antibacterial activity against Gram-negative (P. aeruginosa) and

Gram-positive (*S. aureus*) bacteria and viricidal activity against SARS-COV2. While none of the tested CNMs exhibited any antibacterial activity in suspension, GO and oxidised DWCNTs deposited on silicone exhibited strong antibacterial activity against *P. aeruginosa* and *S. aureus*, respectively. This highlights the impact of the complex interplay between the shape, surface chemistry, and mobility of CNMs on their antibacterial activity. Most available studies of the antimicrobial properties of CNM-containing composites do not detail the exact antimicrobial mechanisms but mainly assume that typical effects of particles free in a liquid medium (essentially oxidative stress) may be transferred to a surface without checking this hypothesis. We have demonstrated here that this assumption is not always true.

As carbon nanomaterials are effectively blocked on the silicone surface and are chemically resistant, we expect no loss of activity with time, while the long-term impact of biofilms will also need to be investigated in further work. The absence of a viricidal effect against SARS-COV2 suggests that considering the possible negative impact of such nanomaterials after inhalation, it may be safer not to include them in respiratory masks in the absence of clear evidence of a real sanitary benefit. This also highlights the need to ban the use of "graphene" as a generic description of 2D carbon-based nanomaterials because very different nanoparticles may be included, such as GO and FLG, exhibiting very different safety concerns.

Data availability

Some of the data supporting this article have been included as part of the ESI.† All data can be made available upon request to the corresponding author (Emmanuel.flahaut@univ-tlse3.fr).

Conflicts of interest

The authors declare no conflict of interest.

Acknowledgements

References

1 M. Cámara, W. Green, C. E. MacPhee, *et al.*, Economic significance of biofilms: a multidisciplinary and cross-sectoral challenge, *npj Biofilms Microbiomes*, 2022, **8**, 42.

2 O. Ciofu, C. Moser, P. Ø. Jensen, *et al.*, Tolerance and resistance of microbial biofilms, *Nat. Rev. Microbiol.*, 2022, **20**, 621–635.

3 D. C. Brown, G. N. Okpala and L. M. Gieg, *et al.*, *Chapter 12 - Biofilms and their role in corrosion in marine environments*, in *Understanding Microbial Biofilms*, 2023, pp. 173–185.

4 Z. K. Zander and M. L. Becker, Antimicrobial and Antifouling Strategies for Polymeric Medical Devices, *ACS Macro Lett.*, 2018, **7**, 16–25.

5 M. Y. Vaidya, A. J. McBain, J. A. Butler, *et al.*, Antimicrobial Efficacy and Synergy of Metal Ions against Enterococcus faecium, Klebsiella pneumoniae and Acinetobacter baumannii in Planktonic and Biofilm Phenotypes, *Sci. Rep.*, 2017, **7**, 5911.

6 B. Pant, P. Pokharel, A. P. Tiwari, *et al.*, Characterization and antibacterial properties of aminophenol grafted and Ag NPs decorated graphene nanocomposites, *Ceram. Int.*, 2015, **41**, 5656–5662.

7 Y. Liu, G. Yang, S. Jin, *et al.*, Development of High-Drug-Loading Nanoparticles, *ChemPlusChem*, 2020, **85**, 2143–2157.

8 C. Dianzani, G. P. Zara, G. Maina, *et al.*, Drug Delivery Nanoparticles in Skin Cancers, *BioMed Res. Int.*, 2014, **2014**, 1–13.

9 P. R. Riley and R. J. Narayan, Recent advances in carbon nanomaterials for biomedical applications: A review, *Curr. Opin. Biomed. Eng.*, 2021, **17**, 100262.

10 A. D. Staneva, D. K. Dimitrov, D. N. Gospodinova, *et al.*, Antibiofouling Activity of Graphene Materials and Graphene-Based Antimicrobial Coatings, *Microorganisms*, 2021, **9**, 1839.

11 V. Popov, Carbon nanotubes: properties and application, *Mater. Sci. Eng., R*, 2004, **43**, 61–102.

12 L. Giraud, A. Tourrette and E. Flahaut, Carbon nanomaterials-based polymer-matrix nanocomposites for antimicrobial applications: a review, *Carbon*, 2021, **182**, 463–483.

13 Y. Liu, M. Park, H. K. Shin, *et al.*, Facile preparation and characterization of poly(vinyl alcohol)/chitosan/graphene oxide biocomposite nanofibers, *J. Ind. Eng. Chem.*, 2014, **20**, 4415–4420.

14 S. Yang, P. Lei, Y. Shan, *et al.*, Preparation and characterization of antibacterial electrospun chitosan/poly (vinyl alcohol)/graphene oxide composite nanofibrous membrane, *Appl. Surf. Sci.*, 2018, **435**, 832–840.

15 J. D. Schiffman and M. Elimelech, Antibacterial Activity of Electrospun Polymer Mats with Incorporated Narrow Diameter Single-Walled Carbon Nanotubes, *ACS Appl. Mater. Interfaces*, 2011, **3**, 462–468.

16 Q. Chen, J. D. Mangadlao, J. Wallat, *et al.*, 3D Printing Biocompatible Polyurethane/Poly(lactic acid)/Graphene Oxide Nanocomposites: Anisotropic Properties, *ACS Appl. Mater. Interfaces*, 2017, **9**, 4015–4023.

17 S. Sayyar, R. Cornock, E. Murray, *et al.*, Extrusion printed graphene/polycaprolactone/composites for tissue engineering, *Mater. Sci. Forum*, 2013, **773**, 496–502.

18 S. Sayyar, E. Murray, B. C. Thompson, *et al.*, Processable conducting graphene/chitosan hydrogels for tissue engineering, *J. Mater. Chem. B*, 2015, **3**, 481–490.

19 Y. Liu, J. Wen, Y. Gao, *et al.*, Antibacterial graphene oxide coatings on polymer substrate, *Appl. Surf. Sci.*, 2018, **436**, 624–630.

20 R. Li, N. D. Mansukhani, L. M. Guiney, *et al.*, Identification and Optimization of Carbon Radicals on Hydrated Graphene Oxide for Ubiquitous Antibacterial Coatings, *ACS Nano*, 2016, **10**, 10966–10980.

21 X. Lu, X. Feng, J. R. Werber, *et al.*, Enhanced antibacterial activity through the controlled alignment of graphene oxide nanosheets, *Proc. Natl. Acad. Sci. U. S. A.*, 2017, **114**, E9793–E9801.

22 M. Papi, V. Palmieri, F. Bugli, *et al.*, Biomimetic antimicrobial cloak by graphene-oxide agar hydrogel, *Sci. Rep.*, 2016, **6**, 1–7.

23 J. Sengupta and C. M. Hussain, The Emergence of Carbon Nanomaterials as Effective Nano-Avenues to Fight against COVID-19, *Materials*, 2023, **16**, 1068.

24 J. Sengupta and C. M. Hussain, Carbon nanomaterials to combat virus: A perspective in view of COVID-19, *Carbon Trends*, 2021, **2**, 100019.

25 R. Soni, S. R. Joshi, M. Karmacharya, *et al.*, Superhydrophobic and Self-Sterilizing Surgical Masks Spray-Coated with Carbon Nanotubes, *ACS Appl. Nano Mater.*, 2021, **4**, 8491–8499.

26 S. Lee, J.-S. Nam, J. Han, *et al.*, Carbon Nanotube Mask Filters and Their Hydrophobic Barrier and Hyperthermic Antiviral Effects on SARS-CoV-2, *ACS Appl. Nano Mater.*, 2021, **4**, 8135–8144.

27 E. Flahaut, R. Bacsa, A. Peigney, *et al.*, Gram-scale CCVD synthesis of double-walled carbon nanotubes, *Chem. Commun.*, 2003, 1442–1443.

28 L. Shahriary and A. A. Athawale, Graphene Oxide Synthesized by using Modified Hummers Approach, *Int. J. Renew. Energ. Environ. Eng.*, 2014, **02**, 58–63.

29 L. Chopinet, C. Formosa, M. P. Rols, *et al.*, Imaging living cells surface and quantifying its properties at high resolution using AFM in QI™ mode, *Micron*, 2013, **48**, 26–33.

30 https://www.jpk.com/app-techonotes-img/AFM/pdf/jpk-tech-quantitative-imaging.14-1.pdf, (n.d.).

31 D. Péricat, S. A. Leon-Icaza, M. Sanchez Rico, *et al.*, Antiviral and Anti-Inflammatory Activities of Fluoxetine in a SARS-CoV-2 Infection Mouse Model, *Int. J. Mol. Sci.*, 2022, **23**, 13623.

32 A. Weibel, D. Mesguich, G. Chevallier, *et al.*, Fast and easy preparation of few-layered-graphene/magnesia powders for strong, hard and electrically conducting composites, *Carbon*, 2018, **136**, 270–279.

33 E. Flahaut, F. Agnoli, J. Sloan, *et al.*, CCVD Synthesis and Characterization of Cobalt-Encapsulated Nanoparticles, *Chem. Mater.*, 2002, **14**, 2553–2558.

34 D. Alsteens, D. J. Müller and Y. F. Dufrêne, Multiparametric Atomic Force Microscopy Imaging of Biomolecular and Cellular Systems, *Acc. Chem. Res.*, 2017, **50**, 924–931.

35 H. Chen, B. Wang, D. Gao, *et al.*, Broad-Spectrum Antibacterial Activity of Carbon Nanotubes to Human Gut Bacteria, *Small*, 2013, **9**, 2735–2746.

36 M. Azizi-Lalabadi, Carbon nanomaterials against pathogens; the antimicrobial activity of carbon nanotubes, graphene/graphene oxide, fullerenes, and their nanocomposites, *Adv. Colloid Interface Sci.*, 2020, **284**, 102250.

37 S. Liu, T. H. Zeng, M. Hofmann, *et al.*, Antibacterial Activity of Graphite, Graphite Oxide, Graphene Oxide, and Reduced Graphene Oxide: Membrane and Oxidative Stress, *ACS Nano*, 2011, **5**, 6971–6980.

38 Q. Xin, H. Shah, A. Nawaz, *et al.*, Antibacterial Carbon-Based Nanomaterials, *Adv. Mater.*, 2018, **31**, 1804838.

39 M. Connolly, G. Moles, F. C. Carniel, *et al.*, Applicability of OECD TG 201, 202, 203 for the aquatic toxicity testing and assessment of 2D Graphene material nanoforms to meet regulatory needs, *NanoImpact*, 2023, **29**, 100447.

40 S. Gurunathan, J. W. Han, A. A. Daye, *et al.*, Oxidative stress-mediated antibacterial activity of graphene oxide and reduced graphene oxide in Pseudomonas aeruginosa, *Int. J. Nanomed.*, 2012, **7**, 5901–5914.

41 S. Liu, L. Wei, L. Hao, *et al.*, Sharper and Faster "Nano Darts" Kill More Bacteria: A Study of Antibacterial Activity of Individually Dispersed Pristine Single-Walled Carbon Nanotube, *ACS Nano*, 2009, **3**, 3891–3902.

42 L. R. Arias and L. Yang, Inactivation of Bacterial Pathogens by Carbon Nanotubes in Suspensions, *Langmuir*, 2009, **25**, 3003–3012.

43 F. Perreault, A. F. de Faria, S. Nejati, *et al.*, Antimicrobial Properties of Graphene Oxide Nanosheets: Why Size Matters, *ACS Nano*, 2015, **9**, 7226–7236.

44 S. Sayyar, Fabrication of 3D structures from graphene-based biocomposites, *J. Mater. Chem. B*, 2017, **5**, 3462–3482.

45 B. Lu, T. Li, H. Zhao, *et al.*, Graphene-based composite materials beneficial to wound healing, *Nanoscale*, 2012, **4**, 2978–2982.

46 Y. Wang, P. Zhang, C. F. Liu, *et al.*, A facile and green method to fabricate graphene-based multifunctional hydrogels for miniature-scale water purification, *RSC Adv.*, 2013, **3**, 9240–9246.

47 N. A. Mohamed and N. A. Abd El-Ghany, Novel aminohydrazide cross-linked chitosan filled with multi-walled carbon nanotubes as antimicrobial agents, *Int. J. Biol. Macromol.*, 2018, **115**, 651–662.

48 M. Gomes, L. C. Gomes, R. Teixeira-Santos, *et al.*, Carbon nanotube-based surfaces: Effect on the inhibition of single- and dual-species biofilms of Escherichia coli and Enterococcus faecalis, *Results Surf. Interfaces*, 2022, **9**, 100090.

49 E. Dague, D. Alsteens, J.-P. Latgé, *et al.*, Chemical Force Microscopy of Single Live Cells, *Nano Lett.*, 2007, **7**, 3026–3030.

50 J. M. Francois, C. Formosa, M. Schiavone, *et al.*, Use of atomic force microscopy (AFM) to explore cell wall properties and response to stress in the yeast Saccharomyces cerevisiae, *Curr. Genet.*, 2013, **59**, 187–196.

51 E. Moskvitina, V. Kuznetsov, S. Moseenkov, *et al.*, Antibacterial effect of carbon nanomaterials: Nanotubes, carbon nanofibers, nanodiamonds, and onion-like carbon, *Materials*, 2023, **16**, 957.

52 M. A. Saleemi, Y. L. Kong, P. V. Yong, *et al.*, An overview of antimicrobial properties of carbon nanotubes-based nanocomposites, *Adv. Pharm. Bull.*, 2021, **12**, 449–465.

53 A. R. Deokar, L.-Y. Lin, C.-C. Chang, *et al.*, Single-walled carbon nanotube coated antibacterial paper: Preparation and mechanistic study, *J. Mater. Chem. B*, 2013, **1**, 2639.

54 S. E. Abo-Neima, H. A. Motaweh and E. M. Elsehly, Antimicrobial activity of functionalised carbon nanotubes against pathogenic microorganisms, *IET Nanobiotechnol.*, 2020, **14**, 457–464.

55 A. M. Díez-Pascual, State of the art in the antibacterial and antiviral applications of carbon-based polymeric nanocomposites, *Int. J. Mol. Sci.*, 2021, **22**, 10511.

56 D. Rogala-Wielgus and A. Zieliński, Preparation and properties of composite coatings, based on carbon nanotubes, for medical applications, *Carbon Lett.*, 2023, 565–601.

57 N. Hadidi and M. Mohebbi, Anti-infective and toxicity properties of carbon-based materials: Graphene and functionalized carbon nanotubes, *Microorganisms*, 2022, **10**, 2439.